

**Efficient phase field simulation of a binary dendritic growth in a forced flow**

C. W. Lan\* and C. J. Shih

*Department of Chemical Engineering, National Taiwan University, Taipei 10617, Taiwan, Republic of China*

(Received 26 February 2003; revised manuscript received 22 May 2003; published 11 March 2004)

Efficient quantitative phase field simulation using an adaptive finite volume method with an antisolal trapping scheme is presented for a binary dendritic growth in a forced flow. For the case of no convection, the calculated results with different interface thickness are examined. It is found that with a proper antisolal trapping flux, a thick interface, but smaller than the diffusion boundary layer, could be used and the solution could approach to the sharp-interface Gibbs-Thompson equation limit in almost all aspects quantitatively. Based on the concentration driving force obtained from the sharp-interface limit of the Wheeler-Boettinger-McFadden (WBM) model, the calculated results are in good agreement with the classic Oseen-Ivantsov solution for the concentration-driven growth in a forced flow. And the selection scaling factor also increases with the external flow as the theoretical prediction.

DOI: 10.1103/PhysRevE.69.031601

PACS number(s): 68.70.+w, 81.30.Fb, 05.70.Ln, 64.70.Dv

**I. INTRODUCTION**

The development of alloy microstructures is important in solidification processing for metallic systems, and its prediction has become an important research topic in physics and materials science. The phase field model has emerged as a powerful tool to simulate such a structure evolution [1–12]. However, limited by computation and inherent numerical nature, the phase field model has encountered many difficulties. One of the most important limitations in the phase field simulation is the interface thickness  $\delta$ . The choice of  $\delta$  needs to be small enough so that the sharp-interface limit can be achieved. However, such a value, which is usually in the order of the microscopic capillary length  $d_0$ , is several orders smaller than the scale of microstructures. On the other hand, the length scale of solutal and thermal boundary layers is also several orders larger than that of microstructures. As a result, such a sharp interface limit is too stringent in a realistic simulation, even with today's supercomputers.

Significant progress has been made by Karma and Rappel [6] for the thin-interface limit that  $\delta$  can be chosen in the same order of the scale of microstructure. In addition, the interface kinetic effects can play no role on the solution. With such an implementation, efficient numerical simulations have been reported to the solution even at low supercoolings [8,11]. The effect of convection has been considered [10,11] and the results agree very well with the Oseen-Ivantsov solution for the temperature-driven growth of a pure material. However, with solutal effects for alloy solidification, the thin-interface limit cannot be adopted due to significant solutal trapping. Moreover, the degree of supercooling, which is decided by liquid and solid tip concentration, is not a given parameter. Therefore, so far the phase field simulations for alloys can only provide qualitative results. Solutions with a small enough  $\delta$  are scattered, and no quantitative comparison has been made. The problem becomes particularly difficult when thermal [12] and convec-

tive effects, which have much larger length scales, are taken into account.

Very recently, Karma [13] proposed an antisolal trapping scheme for the binary phase field simulation. He showed that with the antitrapping scheme the dendrite tip speed as well as the solute profile in the solid for a thin interface can be achieved by using a thick interface thickness. Although there are no extensive illustrations and examinations, the idea of using antisolal trapping seems to shed a light on an efficient and quantitative phase field simulation of alloys.

In this paper we adopt Karma's idea and implement the antitrapping scheme in the Wheeler-Boettinger-McFadden (WBM) model [3] using an adaptive finite volume method [11,12]. We take the dendritic growth of a Cu/Ni alloy in an isothermal environment [5] as examples. The results of different interface thickness are examined first for the dendrite tip radius, tip speed, solute concentrations, and morphology. The comparison with the sharp-interface solution and the classic Ivantsov solution is made. Then, the antitrapping is considered for the thickest interface and the calculated results are further examined showing a good approximation to the thin-interface solution. By applying the antitrapping to the growth in a forced flow using a thick interface, we obtained results having good agreement with the Oseen-Ivantsov solution. This seems to be quite promising for a quantitative phase field modeling.

In Sec. II the model and the adaptive method used are described briefly. Section III is devoted to results and discussion, where detailed comparisons of the solutions from different interface thickness and antitrapping are made. Furthermore, the effect of convection is discussed and the quantitative comparison with the Oseen-Ivantsov solution is made before drawing the conclusion in Sec. IV.

**II. MATHEMATICAL FORMULATION AND NUMERICAL SOLUTION**

The dendritic growth from a small circle seed in a large supercooled Ni/Cu melt at composition  $c_0$  and temperature  $T_0$  under a forced flow, as shown in Fig. 1, is simulated here.

---

\*Corresponding author. FAX: 886-2-2363-3917. Email address: cwlan@ccms.ntu.edu.tw

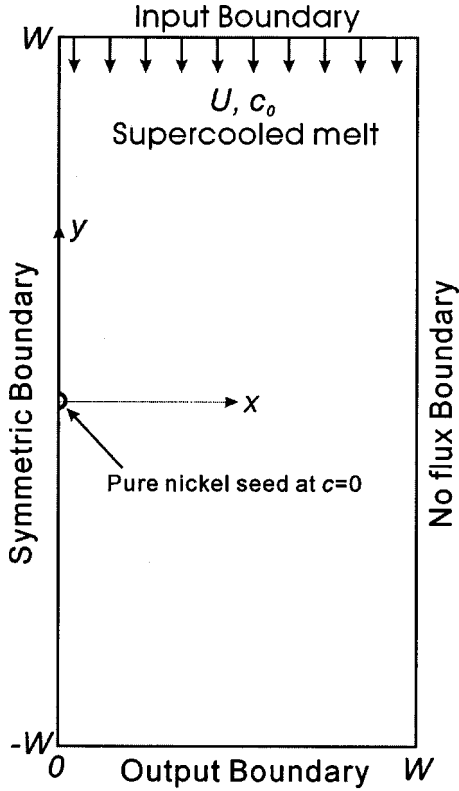


FIG. 1. Computational domain and physical boundary conditions for a binary dendritic growth in a forced flow.

Due to the symmetry, a half domain is considered. For the case of no convection, one can further reduce it into a quarter domain, while setting the far field condition to  $c_0$  and  $T_0$  on the right boundary. In this study, for comparison purposes we have used the isothermal approximation, which is the same as that used by Warren and Boettinger [5], and the growth is mainly driven by concentration. Because the crystallographic directions have been aligned with the coordinate axes, a half domain is adequate for simulation. A sample mesh for the case without convection having the smallest interface thickness ( $\delta = 2 \times 10^{-9}$  m) is shown in Fig. 2(a), where local magnifications of the dendrite tip are illustrated. For the cases with a forced flow in a half domain, a typical mesh is shown in Fig. 2(b). Again, it is shown with three different viewing scales. For comparison purposes, the WBM model [3] is also adopted here, but the antitrapping scheme due to Karma [13] is included. Without antitrapping, the WBM model was proposed by Wheeler, Boettinger, and McFadden [3] using the minimization of a Gibbs free energy function. Based on an entropy function, Penrose and Fife [14] and Warren and Boettinger [5] derived the WBM model for nonisothermal growth. In order to present the governing equations in dimensionless form, the variables are rescaled. The concentration (atomic fraction)  $c$  is rescaled by  $c_0$  to  $c^*$ , where  $c_0$  is the far field concentration. The length, in terms of the coordinates  $x$  and  $y$ , is rescaled by  $l$  to  $x^*$  and  $y^*$ , respectively, and time  $t$  by  $l^2/D_L$  to  $t^*$ , where  $l$  is a characteristic length and  $l^2/D_L$  is a characteristic time;  $D_L$  is the solute diffusivity in the liquid. The phase field variable  $\phi$  is set to be 1 in liquid and 0 in solid, while 0.5 at the interface.

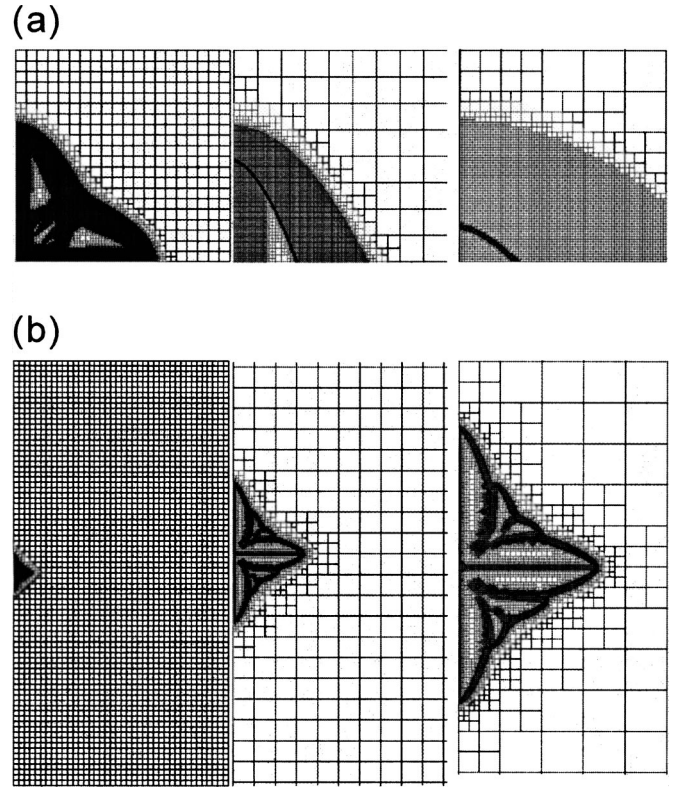


FIG. 2. Adaptive mesh refinement grid structures in (a) diffusive growth ( $\delta = 2 \times 10^{-9}$  m); (b) convective growth ( $\delta = 4.9 \times 10^{-8}$  m).

The velocity  $\mathbf{v}$  is rescaled by  $D_L/l$  to  $\mathbf{v}^*$ . Then, the governing equations used in [5] can be represented in dimensionless form

$$\nabla \cdot \mathbf{v}^* = 0, \quad (1)$$

$$\frac{\partial \mathbf{v}^*}{\partial t^*} + \mathbf{v}^* \cdot \nabla \mathbf{v}^* = Sc \nabla^2 \mathbf{v}^* - \nabla P^* - Sc \frac{l^2}{\delta^2} h(1-\phi)^2 \mathbf{v}^*, \quad (2)$$

$$\begin{aligned} \frac{\partial \phi}{\partial t^*} = & \tilde{M}_\phi^* \tilde{\epsilon}^{*2} \left[ \nabla \cdot (\eta^2 \nabla \phi) - \frac{\partial}{\partial x} \left( \eta \eta_\beta \frac{\partial \phi}{\partial y} \right) \right. \\ & \left. + \frac{\partial}{\partial y} \left( \eta \eta_\beta \frac{\partial \phi}{\partial x} \right) \right] - \tilde{M}_\phi^* \tilde{S}^* \end{aligned} \quad (3)$$

$$\begin{aligned} \frac{\partial c^*}{\partial t^*} + \mathbf{v}^* \cdot \nabla c^* = & \nabla \cdot \{ D^* [\nabla c + c^*(1-c_0 c^*) \\ & \times (S_B^* - S_A^*) \nabla \phi] + \mathbf{j}_a^* \}. \end{aligned} \quad (4)$$

The first two equations are the equation of continuity and the equation of motion, respectively. In the equation of motion,  $Sc \equiv \nu/D_L$  is the Schmidt number, where  $\nu$  is the melt viscosity and assumed to be constant here. The source term is related to the fluid/solid interaction for the two-phase region for the diffusive interface, which was proposed by Beckermann *et al.* [15]. In the rest of equations, the variable with a tilde is the concentration-weighted average. Inside the diffu-

sive interface, the properties are weighted by a function  $p(\phi)$  from a double-well function  $g(\phi)$ , which is defined by  $g(\phi) = \phi^2(1-\phi)^2$ . The weighting function  $p(\phi)$  for the averaged physical properties of the solid/liquid mixture is chosen such that  $p'(\phi) = 30g(\phi)$  [5]. For example, the normalized diffusivity of the solution is given by

$$D^* = D/D(c_0) = [D_s + p(\phi)(D_L - D_s)]/D_L, \quad (5)$$

where the individual diffusivity has been assumed not affected by the solute concentration, e.g.,  $D(c_0) = D_L$ ; both  $D_s$  and  $D_L$  are assumed constant here, i.e.,  $D \equiv \tilde{D}$ . In addition,  $S_A^*$  and  $S_B^*$  are the normalized entropy of  $A$  (solvent) and  $B$  (solute), respectively, being scaled by  $R/V_m$ , i.e.,  $S_i^* = S_i V_m / R$  ( $i=A$  or  $B$ );  $V_m$  is the molar volume and  $R$  the gas constant. The entropies of  $A$  and  $B$  are defined as the following:

$$S_A(\phi, T) = W_A g'(\phi) + p'(\phi) \Delta H_A \left( \frac{1}{T} - \frac{1}{T_m^A} \right), \quad (6)$$

$$S_B(\phi, T) = W_B g'(\phi) + p'(\phi) \Delta H_B \left( \frac{1}{T} - \frac{1}{T_m^B} \right), \quad (7)$$

where  $W_A$  and  $W_B$  are constants and  $T_m^A$  and  $T_m^B$  are the melting points of  $A$  and  $B$ , respectively;  $\Delta H_A$  and  $\Delta H_B$  are the heats of fusion per volume. Again, in Eq. (3),  $\tilde{S}^*$  is the concentration-averaged value, i.e.,  $\tilde{S}^* = (1-c)S_A^* + cS_B^*$ .

The anisotropic function  $\eta$  in Eq. (3) is defined for the fourfold symmetry as

$$\eta = 1 + \gamma \cos(4\beta), \quad (8)$$

where  $\gamma$  is the intensity of the anisotropy and  $\beta = \tan^{-1}[(\partial\phi/\partial y)/(\partial\phi/\partial x)]$  determining the growth orientation of the dendrite. In this study we have purposely chosen (100) is in the  $x$  direction and (010) is in the  $y$  direction, so that the fourfold symmetry allows us to take a half domain for simulation, which saves computational effort significantly. Finally, the dimensionless mobility function  $\tilde{M}_\phi^*$ , being scaled by  $D_L V_m / (Rl^2)$ , is taken from the average of  $M_i = T_m^{i2} \beta_i / (6\sqrt{2} \Delta H_i \delta_i)$ ,  $i=A$  or  $B$ , where  $\beta_i$  is the kinetic coefficient and  $\delta_i$  the interface thickness, which are assumed to be the same for  $A$  and  $B$  here. Similarly,  $\tilde{\epsilon}^{*2}$  is a dimensionless parameter being rescaled by  $l^2$ . For each component,  $\epsilon_i^2 = 6\sqrt{2} \sigma_i \delta_i / T_m^i$ , where  $\sigma_i$  is the interfacial energy. All the parameters chosen are the same as those in [5], which are similar to the ones used in the WBM model [3].

The only difference comparing with the WBM model [3,5] is in the last term of the concentration equation, which is the antitrapping current introduced by Karma [13]. By following Karma's paper [13],  $j_a^*$  can be defined as

$$j_a^* = a \frac{\delta}{l} (1-k) \left[ \frac{2c^*}{1+k-(1-k)h(\phi)} \right] \frac{\partial\phi}{\partial t} \frac{\nabla\phi}{|\nabla\phi|}, \quad (9)$$

where  $a$  is the antitrapping coefficient and needs to be adjusted to fit the solid concentration of the sharp-interface

solution. Also,  $h(\phi) = \phi$  is used such that the condition of conservation of mass is guaranteed; other selections are also possible [13]. Although there are some differences between Karma's model and the WBM model, the choice of  $h(\phi)$  here seems to work quite well in our simulation.

The boundary conditions are straightforward for the above equations. The symmetry condition is used at the centerline. On the right side, the velocity is by the stress-free condition and the concentration constant at  $c_0$ ; the zero-flux condition can also be used for concentration, but the result is the same due to the large domain used. The inlet velocity is given to be  $U$  and the concentration  $c_0$ . The outflow boundary condition is further set by the overall mass balance. The pressure at boundary is then obtained by linear extrapolation from the interior points.

We start the simulation from a pure nickel seed with an initial radius  $2l$ . During growth, the mesh is adapted along the interface and high concentration-gradient regions;  $0.05 < \phi < 0.95$  and  $0.1 < |\nabla c|$  are chosen for mesh refinement. For the time integration, all variables are treated by the first-order fully implicit Euler method, while a second-order finite volume scheme is applied to the space domain. For the cases with fluid flow, SIMPLE scheme based on pressure correlation used [16]. The finite volume method is simple and straightforward. For a domain, one can generate a number of square finite volumes with faces in conjunction to its neighbor cells. Then, the integration of the conservation equations over each finite volume, with Gauss theorem, flux balance equations can be obtained for each cell.

In order to have a large domain for calculation, while keeping the cells near the interface to be small enough, adaptive mesh refinement (AMR) is necessary. Provatas, Goldenfeld, and Dantzig [8] proposed an efficient adaptive finite element method for simulation, and the ratio of the largest to smallest cell size was up to  $2^{17}$ . Their computing cost scales with domain size ( $L^2$ ). Adaptive meshes were also considered by Braun [17] and Amberg [9,18]. Recently, Jeong *et al.* further developed a three-dimensional (3D) AMR [19] for a dendritic growth of a pure material at high supercooling. We have also developed an efficient AMR scheme based on the finite volume method for dendritic growth [11,16]. The details of the adaptive finite volume method can be found elsewhere [16]. The scheme has also been applied to a nonisothermal diffusive growth (without convection and antitrapping) as well [12]. In our AMR scheme, or simplicity, we have adopted a simple way to do refinement using quadrilateral cells. Sample meshes are shown in Fig. 2. In short, for the refinement, the parent cell is subdivided into four kid cells, while for coarsening, the kid cells are deleted. Constructing the data structure is straightforward by using pointers and derived data types of FORTRAN 90. Detailed description of the adaptive data structure and a sample programming can be found elsewhere [16].

### III. RESULTS AND DISCUSSION

For comparison purposes, the Ni/Cu system used by Warren and Boettinger [5] is considered here. The physical properties and the system related parameters, unless otherwise

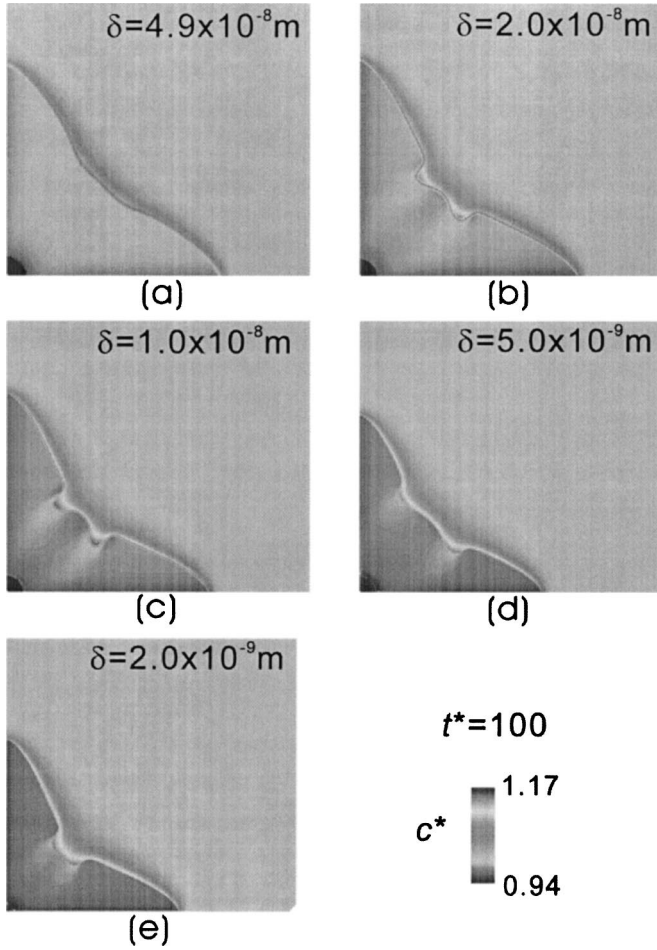


FIG. 3. Growth morphologies and solute fields at different interface thickness for diffusive growth: (a)  $\delta = 4.9 \times 10^{-8}$  m; (b)  $\delta = 2 \times 10^{-8}$  m; (c)  $\delta = 1 \times 10^{-8}$  m; (d)  $\delta = 5 \times 10^{-9}$  m; (e)  $\delta = 2 \times 10^{-9}$  m. The calculations stop at  $t^* = 100$ .

stated, are the same as those in [5];  $T_{\text{ref}} = 1594.5$  K,  $T_0 = 1574$  K,  $c_0 = 0.4083$ ,  $\gamma = 0.04$ , and time step  $\Delta t^* = 0.2$ , etc., as well as those parameters used in the WBM model;  $\beta_A = 0.33 \times 10^{-2}$  m/(K s),  $\beta_B = 0.39 \times 10^{-2}$  m/(K s),  $L_A = 2350 \times 10^6$  J/m<sup>2</sup>,  $L_B = 1728 \times 10^6$  J/m<sup>2</sup>,  $\sigma_A = 0.37$  J/m<sup>2</sup>, and  $\sigma_B = 0.29$  J/m<sup>2</sup>. Different interface thickness ( $\delta = 2 \times 10^{-9} \sim 4.9 \times 10^{-8}$  m) are chosen for comparison for diffusive growth, and the adaptive mesh for the smallest interface thickness ( $\delta = 2 \times 10^{-9}$  m) is shown in Fig. 2(a). The characteristic length  $l = 4.606 \times 10^{-8}$  m and the smallest cell size  $\Delta x_{\text{min}} = 1.497 \times 10^{-9}$  m are chosen here; the smallest cell size used here is also much smaller than that used before [5,9]. For  $\delta = 2 \times 10^{-9}$  m, the domain  $W = 100l$  is the smallest one and the simulation stops at  $t^* = 100$ , which corresponds to 0.212 ms in real time. In all cases, the tip speed reaches to a steady state when  $t^* \sim 30$ . For other cases,  $W = 750l$  has been used. Due to the use of the small interface thickness, the computation time increases with the decreasing  $\delta$ . For the smallest  $\delta$ , the calculation takes about a week, which will be discussed shortly. The calculated morphologies using different interface thickness are shown in Fig. 3. As shown, the calculated morphologies are very different, and

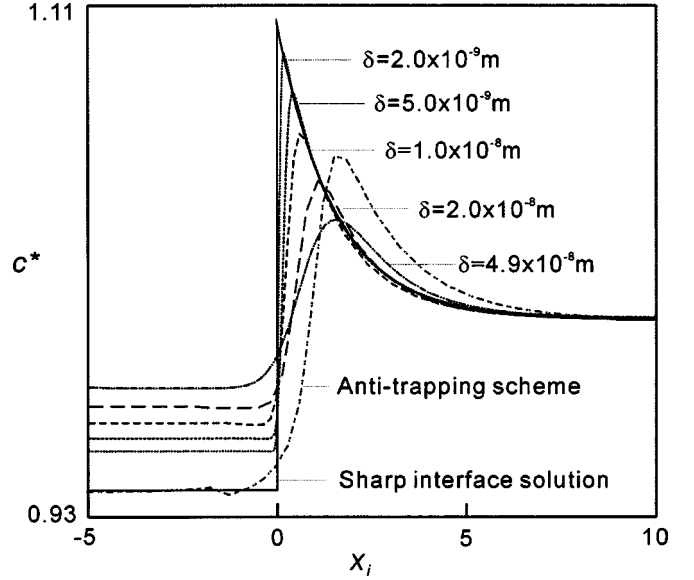


FIG. 4. Calculated solute distributions for different interface thickness along the centerline of the dendrite tip. The sharp interface concentrations are obtained by Eq. (10).

dendrite grows slower when the interface thickness  $\delta$  is reduced. The concentration buildup also increases with the decreasing  $\delta$ . Moreover, the concentration profiles along the tip for different  $\delta$ 's are shown in Fig. 4. As shown, with the decrease of the interface thickness, the sharp interface limit can be approached, where the tip concentrations are obtained from the asymptotic limit of the WBM model [3,5]:

$$\begin{aligned} & \frac{V}{\beta^A \eta(\theta)} + \frac{\kappa \sigma^A [\eta(\theta) + \eta''(\theta)] T_m^A}{L^A} \\ &= \left( \frac{(T_m^A)^2}{T} - T_m^A \right) + \frac{R_g (T_m^A)^2}{V_m L^A} \ln \frac{1 - C_L^{\text{SI}}}{1 - C_S^{\text{SI}}}, \\ & \frac{V}{\beta^B \eta(\theta)} + \frac{\kappa \sigma^B [\eta(\theta) + \eta''(\theta)] T_m^B}{L^B} \\ &= \left( \frac{(T_m^B)^2}{T} - T_m^B \right) + \frac{R_g (T_m^B)^2}{V_m L^B} \ln \frac{C_L^{\text{SI}}}{C_S^{\text{SI}}}, \end{aligned} \quad (10)$$

where  $V$  is the dendrite tip speed,  $\beta^A$  and  $\beta^B$  are the kinetic coefficients of the solvent and the solute,  $L^A$  and  $L^B$  are the

TABLE I. Calculated interface concentrations and segregation coefficients for various interface thickness; the antitrapping results are based on  $\delta = 4.9 \times 10^{-8}$  m.

$\delta$ (m)	$C_L^{\text{SI}}$	$C_S^{\text{SI}}$	$C_L$	$C_S$	$C_L/C_L^{\text{SI}}$	$C_S/C_S^{\text{SI}}$	$k$
$4.9 \times 10^{-8}$	1.108	0.945	1.035	0.976	0.934	0.881	0.943
$2.0 \times 10^{-8}$	1.105	0.942	1.049	0.969	0.949	0.877	0.924
$1.0 \times 10^{-8}$	1.104	0.941	1.065	0.963	0.965	0.872	0.904
$5.0 \times 10^{-9}$	1.104	0.940	1.080	0.958	0.978	0.868	0.887
$2.0 \times 10^{-9}$	1.105	0.941	1.093	0.953	0.989	0.862	0.872
Antitrapping	1.110	0.946	1.058	0.940	0.953	0.847	0.888

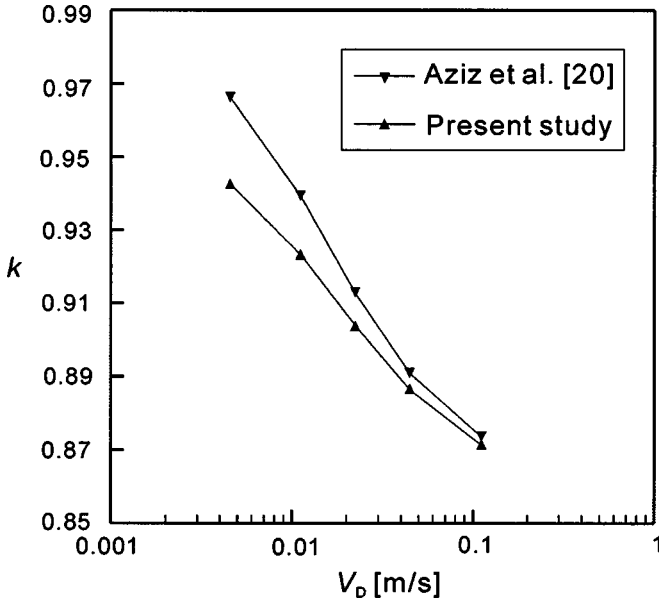


FIG. 5. The calculated segregation coefficients, with solute trapping, as a function of the diffusion velocity  $V_D$  [21] and the comparison with the results by Aziz *et al.* [20].

latent heat,  $\sigma^A$  and  $\sigma^B$  are the interfacial energy, and  $\kappa$  is the tip curvature. In Fig. 4 the shape-interface concentration profile in the melt is obtained by an exponential function. In Eq. (10), if the kinetic coefficients are infinity, the equation is precisely the Gibbs-Thomson equation. However, in Eq. (10), if we want to calculate the concentrations for the sharp interface limit in addition to the tip speed  $V$ , an accurate estimation of the local tip radius  $\rho$  (or  $1/\kappa$ ) is necessary. To do so, we have adopted a fourth-order polynomial to fit the tip within  $3l$ , the calculated tip radii and other values extracted from the simulation for various  $\delta$ 's are listed in Table I for comparison. The calculated segregation coefficients for different  $\delta$ 's also follow nicely with the model by Aziz *et al.* [20], i.e.,  $k_v = (k + V/V_D)/(1 + V/V_D)$ , where  $V_D = 0.207[D_L \ln(1/k)/\delta(1-k)]$  [21], as shown in Fig. 5.

With the tip speed, radius (local one), and concentrations, the growth Peclet number  $P_C = \rho V/2D_L$  and the normalized growth driving force  $\Delta_{\text{mod}} = (C_L - C_L^\infty)/(C_L - C_S)$  based on the phase field model can be evaluated, where  $C_L$  and  $C_S$  are the tip concentrations at the liquid and solid sides, respectively, and  $C_L^\infty$  is the concentration at infinity in the melt.

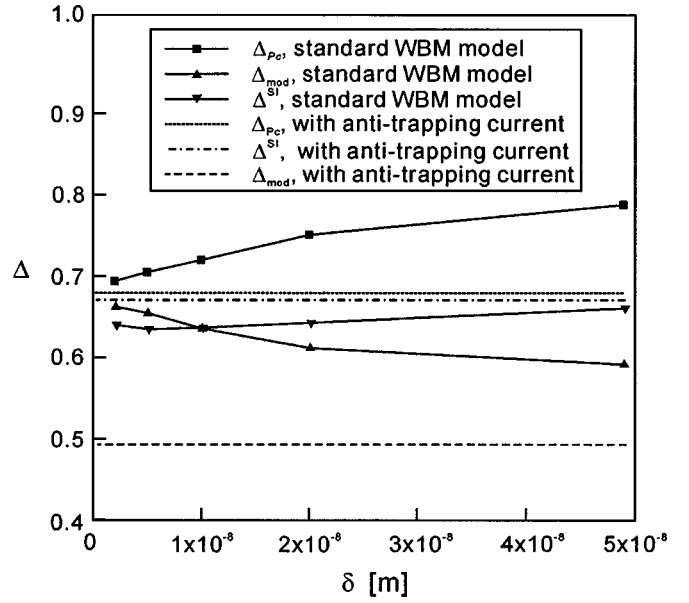


FIG. 6. Various normalized concentration driving forces as a function of the interface thickness.

With  $P_C$  and  $\Delta_{\text{mod}}$ , the comparison with the classic Ivantsov solution [22] is possible. If we have a  $P_C$ , the driving force  $\Delta_{P_C}$  based on the Ivantsov solution can also be obtained:

$$\Delta_{P_C} = \sqrt{\pi P_C} \exp(P_C) \text{erfc}(\sqrt{P_C}). \quad (11)$$

However, this equation is correct only for  $\sigma^A = \sigma^B = 0$  and  $\beta^A$  and  $\beta^B$  are infinity. Similarly, based on Eq. (10), which is the sharp-interface solution of the WBM model, one can calculate another driving force, which can be denoted as  $\Delta^{\text{SI}} = (C_L^{\text{SI}} - C_L^\infty)/(C_L^{\text{SI}} - C_S^{\text{SI}})$ ; SI stands for the sharp interface. The comparison of these three driving forces is illustrated in Table II, as well as in Fig. 6. As shown, the maximum inconsistency between  $\Delta_{P_C}$  and  $\Delta^{\text{SI}}$  with the Ivantsov model for the smallest interface thickness ( $\delta = 2 \times 10^{-9}$  m) is only about 8%, while the agreement between  $\Delta_{\text{mod}}$  and  $\Delta^{\text{SI}}$  is also reasonable. Furthermore, the results in Table II are consistent with those obtained by Warren and Boettinger [5], but they were not be able to solve the whole dendrite by using the smallest interface thickness. We also put the overall tip radius in Table II for comparison. In general, the overall den-

TABLE II. Calculated tip radii, Peclet numbers, and normalized concentration driving forces for various interface thickness; the antitrapping results are based on  $\delta = 4.9 \times 10^{-8}$  m.

$\delta$ (m)	Overall $\rho(l)$	$\rho(l)$	$V(D_L/l)$	$P_C$	$\Delta_{P_C}$	$\Delta_{\text{mod}}$	$\Delta^{\text{SI}}$	Error <sup>a</sup>
$4.9 \times 10^{-8}$	14.793	3.817	0.656	1.252	0.788	0.593	0.661	19.19%
$2.0 \times 10^{-8}$	9.091	2.839	0.669	0.950	0.751	0.613	0.643	16.78%
$1.0 \times 10^{-8}$	6.954	2.464	0.621	0.765	0.720	0.637	0.637	13.05%
$5.0 \times 10^{-9}$	5.097	2.393	0.579	0.693	0.705	0.656	0.635	11.02%
$2.0 \times 10^{-9}$	4.690	2.349	0.545	0.640	0.694	0.664	0.640	8.32%
Antitrapping	4.921	2.447	0.500	0.612	0.687	0.492	0.671	2.38%

<sup>a</sup>The relative error is obtained for  $\Delta_{P_C}$  by using  $\Delta^{\text{SI}}$  as the reference, i.e.,  $\text{error} = (\Delta_{P_C} - \Delta^{\text{SI}})/\Delta^{\text{SI}}$ .

TABLE III. Computational comparison for various interface thickness and the antitrapping case at  $t^* = 100$ .

$\delta$ (m)	Domain size ( $l^2$ )	$\Delta x_{\max}$ ( $l$ )/level	$\Delta x_{\min}$ ( $l$ )	$\Delta t$ ( $l^2/D_L$ )	Total grids	CPU time (hr)
$4.9 \times 10^{-8}$	$750 \times 750$	10/5	0.625	0.2	8004	0.21
$2.0 \times 10^{-8}$	$750 \times 750$	10/6	0.3125	0.1	15 915	0.65
$1.0 \times 10^{-8}$	$750 \times 750$	10/7	0.15625	0.05	21 033	3.92
$5.0 \times 10^{-9}$	$750 \times 750$	10/8	0.078125	0.02	42 510	23.82
$2.0 \times 10^{-9}$	$100 \times 100$	10/9	0.0390625	0.005	113 485	175.75
Antitrapping	$750 \times 750$	10/6	0.3125	0.2	14 325	0.43

drite tip radius is about twice larger than the local one. Because the solutal boundary layer is only a few  $l$ , and the tip concentration is affected by the local tip radius, the use of the local tip is found to be more reasonable for the Ivantsov solution as a whole. Furthermore, as shown in Fig. 6, with the decreasing interface thickness, the normalized driving forces seem to converge to a range near 0.67. Similarly, this is consistent with Fig. 3 that the dendrite tip shape and speed converge with the decreasing interface thickness. However, the computation time for this case with the smallest interface thickness ( $\delta = 2 \times 10^{-9}$  m) is tremendously long already, and further reducing the interface thickness is unrealistic. The domain size, maximum cell size/level of mesh, minimum cell size, time step size, the total cell number used at  $t^* = 100$ , and the CPU time used are listed in Table III for comparison. As shown, the number of total cells and the CPU time increase rapidly as the interface thickness is reduced. Also, the time step size needs to be reduced for a smaller  $\delta$  to ensure numerical stability.

In order to reduce the CPU time, while showing the possibility of obtaining a reasonable solution, we have chosen the largest  $\delta$  for the simulation with the antitrapping current. The antitrapping coefficient  $a = 1/\sqrt{2}$ , which is twice of Karma's choice [13] in Eq. (9) is picked by matching the solid concentration obtained by Eq. (10), i.e., the sharp-interface limit. Surprisingly, the calculated morphology agrees very well with the one obtained by using the smallest  $\delta$  in Fig. 3, as shown in Fig. 7, at  $t^* = 100$ . The calculated values in

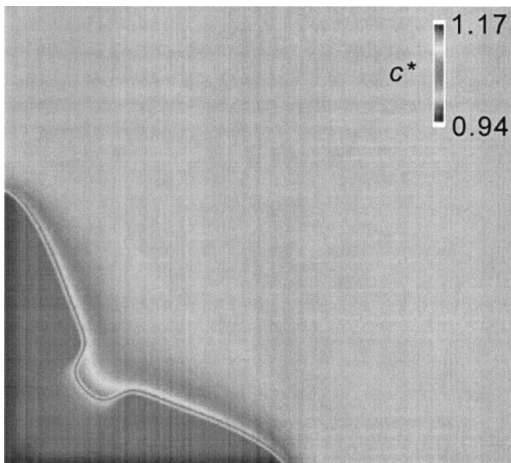


FIG. 7. Calculated growth morphology and solute field at  $t^* = 100$  for  $\delta = 4.9 \times 10^{-8}$  m with the antisolute trapping current.

Tables I and II also show that the results obtained from the antitrapping scheme gives good consistency in the driving forces with the thin-interface solution, except  $\Delta_{\text{mod}}$ . Besides, the CPU time for calculating the antitrapping flux is quite trivial. Interestingly enough, as we have seen the large difference in the dendrite morphology for different  $\delta$ 's in Fig. 3, the difference at later time, say  $t^* = 500$ , is even larger, as illustrated in Fig. 8 for the ones with and without the antitrapping current; the one with antitrapping is assumed to have a similar morphology as the one with  $\delta = 2 \times 10^{-9}$  m. The more morphological features of the antitrapping solution are believed to be the cause of the larger solutal driving force. Again, in both cases, no noise has been introduced.

Nevertheless, if we examine the concentration profile alone the dendrite center in Fig. 4, this antitrapping scheme fails to give a good concentration distribution in front of the dendrite tip. The maximum tip concentration is pumped up by the antitrapping current, while the whole profile is pushed forward to the melt side as well. As a result, its  $\Delta_{\text{mod}}$ , as shown in Fig. 6, is the worst among all cases. Indeed, its maximum tip concentration is too low for a reasonable prediction of the driving force  $\Delta_{\text{mod}}$ . However, other features, such as the tip speed and radius, seem to be good enough for our needs. Fortunately, since the tip speed and radius can be correctly estimated, getting a right tip concentration is straightforward by using Eq. (10). If we do so, the solution happens to be quite satisfactory. The agreement with the Ivantsov solution seems to be quite good as well, as shown in Fig. 6. From this, it may be appropriate to conclude that the antitrapping scheme amends the problem due to the thick interface, while the solution behavior away from the inter-

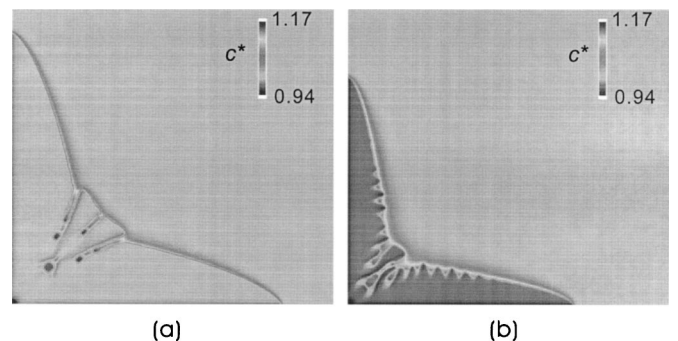


FIG. 8. Comparison of the growth morphologies and solute fields at  $t^* = 500$ : (a) without the antisolute trapping current, (b) with the antisolute trapping current.

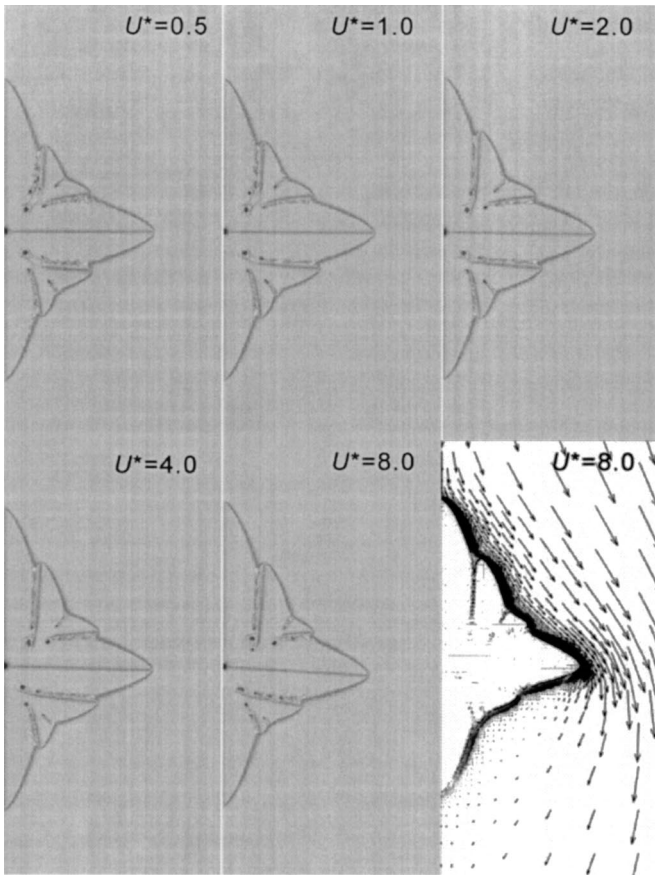


FIG. 9. Calculated growth morphologies and solute fields at  $t^* = 500$  for various external flow velocities without the antisolute trapping current;  $\delta = 4.9 \times 10^{-8}$  m.

face is not much affected. If this argument can be accepted, a more complicated and realistic problem, such as nonisothermal and convective growth, can be solved easily by using the same antitrapping coefficient.

After building the confidence for the diffusive growth, the antitrapping scheme is applied to study the effect of convection on the growth, which is a much more difficult problem from the computation point of view. The domain required for convective growth should be much larger due to the large momentum boundary layer thickness  $\delta_m$ , which can be estimated by

$$\delta_m \approx \frac{\nu}{V} = \frac{6.25 \times 10^{-7} \text{ m}^2/\text{s}}{0.015 \text{ m/s}} = 4.1 \times 10^{-5} \text{ m} \sim 1000l, \tag{12}$$

where  $\nu$  is the kinetic viscosity and  $V$  is the steady-state tip speed. Based on this approximation, the domain size of  $8000 \times 4000l^2$  is chosen. A computation using such a large domain is formidable for a small  $\delta$  or using a structured mesh. With out adaptive scheme, the problem can be solved in 70 000 cells with  $\Delta x_{\min} = 0.3125l$  at  $t = 500^*$ , but  $\delta$  cannot be too small ( $\delta = 4.9 \times 10^{-8}$  m). Figure 9 shows the morphologies and the concentration profiles calculated by the standard WBM model at  $t^* = 500$  under various external flow velocities. A small window of  $1000 \times 500l^2$  is used for

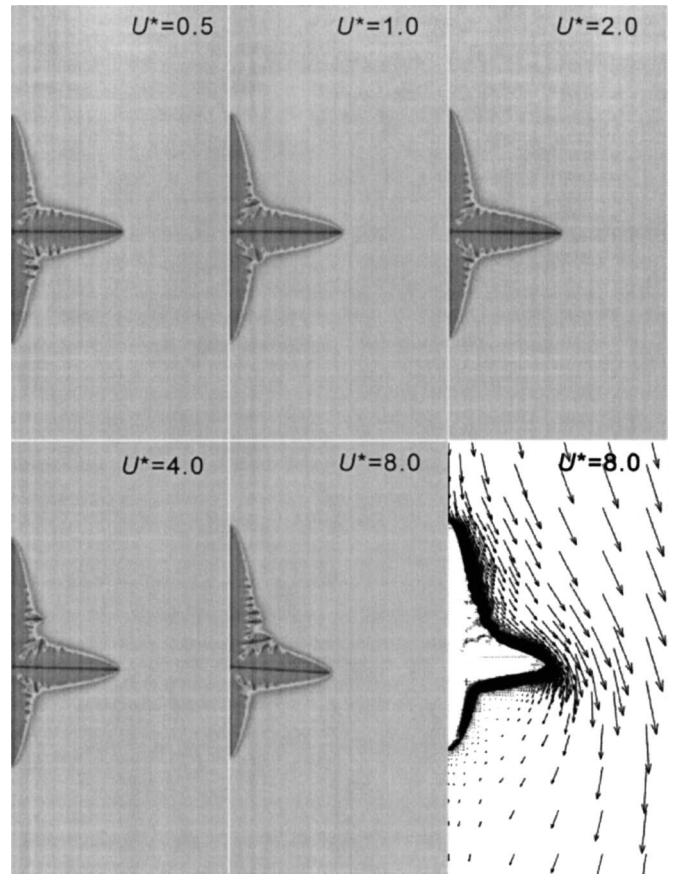


FIG. 10. Calculated growth morphologies and solute fields at  $t^* = 500$  for various external flow velocities with the antisolute trapping current;  $\delta = 4.9 \times 10^{-8}$  m.

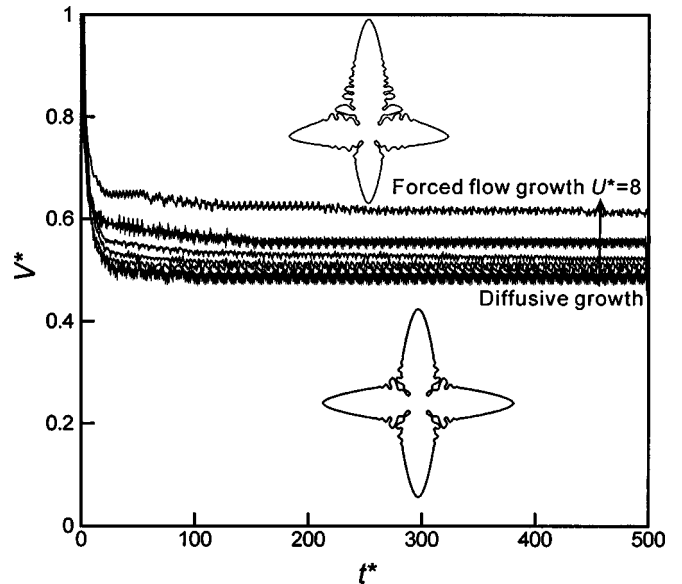


FIG. 11. Calculated upstream tip grow speeds in the presence of different external flow velocities with the antisolutal trapping current; the lines from the bottom are  $U^* = 0, 1, 2, 4, 6,$  and  $8$ , respectively.

better illustration in Fig. 9. The flow field around the dendrite for  $U^* = 8$  is also illustrated in the last plot. Figure 10 shows similar results, but with the antitrapping flux. Again, both results are quite different, and the solute trapping in Fig. 9 leads to a much smaller concentration buildup in the growth front. In both figures, it is clear that the tip growth speed increases with the external velocity which is simply due to the thinner boundary layer in a stronger flow, and the upstream tip growth speed reaches steady state near  $t^* = 100$  because of the fully developed solutal boundary layer as shown in Fig. 11. Besides, in Fig. 9 we can see that the side branchings have preferred growth orientations. Near the upstream arm, the side branches grow upward, and the ones in the downstream side grow transversely. In addition, the primary

sidearm normal to the flow direction is lopsided, and it becomes more significant with the increasing flow velocity. Such a lopsided arm was also observed in experiments [23].

The lopsided arm is also observed in Fig. 10 with the antitrapping current. In addition to the slower growth rate, the major side arms in the grooves disappear. Instead, more small side branches are induced with a stronger forced flow along the upstream dendrite primary arms. They are believed to be the cause of the larger concentration gradients and faster forced flows that contribute more to the morphological instability. Furthermore, an extension of the Ivantsov solution to the convective growth is also possible. Similar to that derived by Bouissou and Pelce [24], the Oseen-Ivantsov solution for a concentration-driven growth in a forced flow can be written as

$$\Delta_{P_C} = P_C \exp(P_C - P_f) \int_1^\infty \frac{\exp\{-P_C \eta + P_f [2 + \int_1^\eta g(\zeta) / \sqrt{\zeta} d\zeta - \eta]\}}{\sqrt{\eta}} d\eta \quad (13)$$

where  $P_f$  is the flow Peclet number defined by  $U\rho/2D_L$ , and

$$g(\zeta) = \frac{\sqrt{\zeta} \operatorname{erfc}(\sqrt{\operatorname{Re} \zeta/2}) + \sqrt{2/(\pi \operatorname{Re})} [\exp(-\operatorname{Re}/2) - \exp(-\operatorname{Re} \zeta/2)]}{\operatorname{erfc}(\sqrt{\operatorname{Re}/2})},$$

where  $\operatorname{Re} = U\rho/\nu$  is the Reynold's number. The solution of this implicit equation is simple and straightforward. The calculated tip velocities, solute concentrations, tip radii, and related values are shown in Table IV for the cases with and without the antitrapping current. Again, because the solute concentration at the sharp-interface limit cannot be accurately estimated by both calculations, we have to recover the values using Eq. (10). As such, the shape-interface driving force  $\Delta^{\text{SI}}$  is calculated. Finally, we can compare our calculations with the Oseen-Ivantsov solution in Fig. 12. As shown, a much better agreement with the classical theory is obtained for the calculations using the antitrapping flux than that by the original WBM model; there is about 40% error for the original WBM model without the antitrapping current. Furthermore, it should be noticed that unlike the temperature-driven growth, the driving force here is not unknown *a priori*, and it is a part of solution for the concentration-driven growth. Without a good concentration calculation, the prediction of the tip speed and morphology is not possible.

The Oseen-Ivantsov solution provides the relationship between  $P_C$  and the driving force  $\Delta$ . However, the solution alone cannot determine the tip speed  $V$  and tip radius  $\rho$  uniquely. According to the stability analysis, Langer *et al.* [1] found an additional equation showing that the scaling factor  $\sigma^* = 2d_0 D/\rho^2 V$  is a property-dependent constant for the dendritic growth of a pure substance. This criterion postulates that a dendrite tip grows at the margin of the stability. A further analysis by Kessler and Levine [25] also pointed out that the steady state solution is not possible except the anisotropy is introduced. Lipton *et al.* [26] also derived the marginal solvability theory for binary alloy, and the scaling

factor  $\sigma^*$  is a function of  $c_L^\infty$  only. In addition, the ratio of the scaling factors, i.e.,  $(\sigma^*)_0/\sigma^*$ , without and with fluid flow is a function of a dimensionless group  $\chi$ ;  $\chi = a(\operatorname{Re})IU/(\gamma^{3/4}\rho V)$ , where  $a(\operatorname{Re}) = \sqrt{2 \operatorname{Re}/\pi} \exp(-\operatorname{Re}/2)/\operatorname{erfc}(\sqrt{\operatorname{Re}/2})$ . It has the form of  $(\sigma^*)_0/\sigma^* \cong 1 + b\chi^{11/14}$  [24], where  $b$  is a constant. If  $\chi$  is small enough (the forced flow is weak), this ratio should be independent of the flow velocity as shown in Fig. 13, which is in good agreement with the prediction of the linearized solvability theory [24]. Also, in the cases of strong external flow,  $(\sigma^*)_0/\sigma^*$  increases slowly both in the standard WBM model and our present antitrapping calculations. The information of scaling factors also shows good agreement with the previous theory for the dendritic growth of a pure substance [10].

Furthermore, unlike the temperature-driven growth [11], the solutal boundary layer is very thin here (about several  $l$ ) and the tip concentration is associated with the local tip radius. The use of an overall dendrite shape for calculating the tip radius cannot restore the assumption used in the Oseen-Ivantsov solution, where a parabolic tip is assumed. Therefore, the use of the local tip radius happens to be necessary for getting a good agreement here. The overall dendrite tip radius is about two times larger than the local one. Again, as mentioned previously, the estimation of the local tip radius is also not trivial. The fourth order polynomial gives the best and consistent fitting to the tip morphology.

#### IV. CONCLUSIONS

An efficient and quantitative phase field simulation using an antisolal trapping scheme is presented for a

TABLE IV. Calculated values from the upstream tip in convective growth using (a) the standard WBM model and (b) with the antisolute trapping current.

$U(D_L/l)$	$V(D_L/l)$	$C_L$	$C_S$	$\Delta_{\text{mod}}$	Overall $\rho(l)$	$\rho(l)$
(a)						
0.5	0.651	1.036	0.977	0.610	15.77	3.846
1.0	0.655	1.033	0.977	0.589	15.53	3.820
2.0	0.662	1.035	0.977	0.603	15.63	3.870
4.0	0.677	1.031	0.977	0.574	15.87	3.990
8.0	0.705	1.031	0.977	0.574	17.24	4.181
16.0	0.750	1.026	0.977	0.531	21.28	4.794
$U(D_L/l)$	$C_L^{\text{SI}}$	$C_S^{\text{SI}}$	$P_C$	$P_f$	$\Delta^{\text{SI}}$	$P_C^I$
0.5	1.112	0.948	1.252	0.962	0.683	0.609
1.0	1.112	0.948	1.251	1.910	0.683	0.634
2.0	1.111	0.948	1.281	3.870	0.681	0.685
4.0	1.111	0.947	1.351	7.980	0.677	0.786
8.0	1.110	0.946	1.474	16.724	0.671	0.968
16.0	1.109	0.945	1.798	38.352	0.665	1.318
(b)						
$U(D_L/l)$	$V(D_L/l)$	$C_L$	$C_S$	$\Delta_{\text{mod}}$	Overall $\rho(l)$	$\rho(l)$
0.5	0.503	1.062	0.941	0.512	5.94	2.446
1.0	0.505	1.059	0.941	0.500	5.96	2.426
2.0	0.523	1.064	0.941	0.520	5.99	2.456
4.0	0.559	1.061	0.940	0.504	6.05	2.476
8.0	0.617	1.054	0.939	0.470	5.88	2.434
$U(D_L/l)$	$C_L^{\text{SI}}$	$C_S^{\text{SI}}$	$P_C$	$P_f$	$\Delta^{\text{SI}}$	$P_C^I$
0.5	1.112	0.948	0.615	0.612	0.683	0.607
1.0	1.112	0.948	0.613	1.213	0.683	0.620
2.0	1.112	0.948	0.642	2.456	0.683	0.651
4.0	1.112	0.948	0.692	4.952	0.683	0.724
8.0	1.109	0.944	0.751	9.736	0.661	0.775

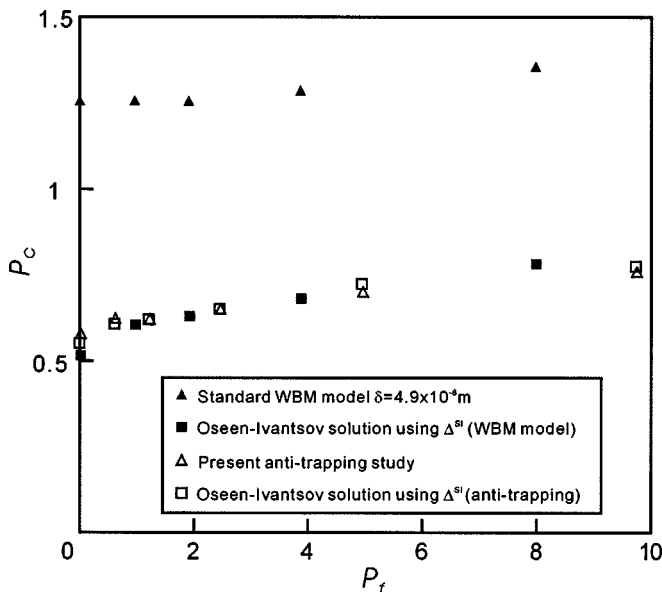


FIG. 12. Comparison of the calculated growth Pelet number as a function of the flow Pelet number with the Oseen-Ivantsov solution.

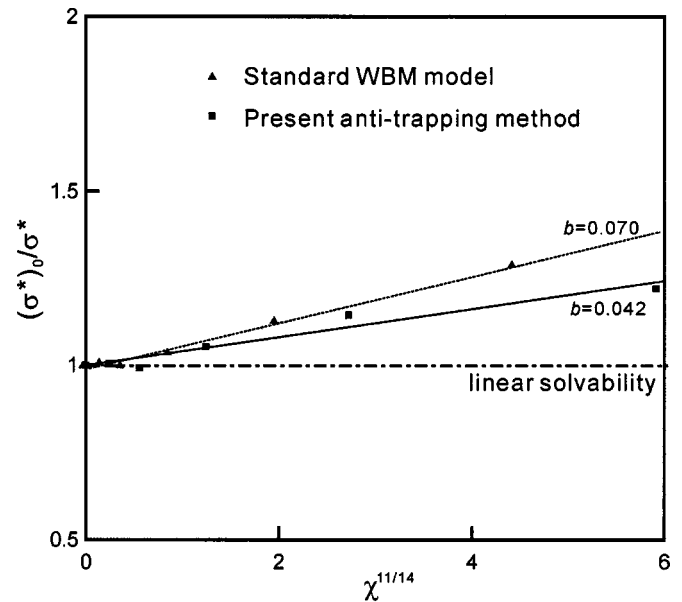


FIG. 13. Comparison of the calculated scaling factor  $(\sigma^*)_0/\sigma^*$  as a linear dependence of the dimensionless group  $\chi^{11/14}$  with the linear solvability theory.

concentration-driven growth of a binary Ni/Cu dendrite in a forced flow. For diffusive growth, several interface thicknesses have been examined and compared with the sharp-interface limit and the classic Ivantsov solution, and good agreement is obtained. It is clear that due to solutal trapping, the driving force for the growth is difficult to compute accurately, so are the dendrite tip radius and speed. Such errors decrease with the decreasing interface thickness, but unfortunately the computational cost also increases rapidly. Thus, for a realistic and quantitative simulation in a large domain, it is extremely difficult to use a thin interface. By using an antitrapping flux, the limitation on the interface thickness can be much relaxed. The calculated growth speed and solute concentration in the solid side, as well as the dendrite morphology, are in good agreement with those obtained by using a much thinner interface. However, the tip solute concentration in the melt side remains to be small as compared with

the thin-interface solution. Nevertheless, if one can restore the concentration from the sharp-interface limit of the WBM model, a good and consistent agreement with the theory can be obtained. Such an agreement is also found for the growth in a forced flow, which requires a much larger computational domain. Moreover, the dimensionless scaling factor ratios are linear proportional to the flow parameter  $\chi^{11/14}$ , which is in good agreement with previous analytical study. The use of the antitrapping scheme indeed reduces computation costs by several orders and opens a window for a realistic and quantitative alloy phase field simulation.

#### ACKNOWLEDGEMENT

This research is sponsored by the National Science Council of the Republic of China.

- 
- [1] J. S. Langer, in *Chance and Matter*, Lecture on the Theory of Pattern Formation, Les Houches XLVI, edited by J. Souletie, J. Vannimenus, and R. Stora (North-Holland, Amsterdam, 1987), pp. 629–711.
- [2] G. Caginap and P. Fife, *Phys. Rev. B* **33**, 7792 (1986).
- [3] A. A. Wheeler, W. J. Boettinger, and G. B. MacFadden, *Phys. Rev. A* **45**, 7424 (1992); *Phys. Rev. E* **47**, 1893 (1993).
- [4] G. Caginalp and W. Xie, *Phys. Rev. E* **48**, 1897 (1993).
- [5] J. A. Warren and W. J. Boettinger, *Acta Metall. Mater.* **43**, 689 (1995).
- [6] A. Karma and W. J. Rappel, *Phys. Rev. E* **53**, R3017 (1996); **57**, 4323 (1998).
- [7] S. G. Kim, W. T. Kim, and T. Suzuki, *Phys. Rev. E* **60**, 7186 (1999).
- [8] N. Provatas, N. Goldenfield, and J. Dantzig, *Phys. Rev. Lett.* **80**, 3308 (1998).
- [9] I. Loginova, G. Amberg, and J. Argen, *Acta Mater.* **49**, 573 (2001).
- [10] X. Tong, C. Beckermann, and A. Karma, *Phys. Rev. E* **61**, 49 (2000).
- [11] C. W. Lan, C. M. Hsu, and Y. C. Chang, *Phys. Rev. E* **65**, 061601 (2002).
- [12] C. W. Lan, Y. C. Chang, and C. J. Shih, *Acta Mater.* **51**, 1857 (2003).
- [13] A. Karma, *Phys. Rev. Lett.* **87**, 115701 (2001).
- [14] O. Penrose and P. C. Fife, *Physica D* **43**, 44 (1990).
- [15] C. Beckermann, H.-J. Diepers, I. Steinbach, A. Karma, and X. Tong, *J. Comput. Phys.* **154**, 468 (1999).
- [16] C. W. Lan, C. C. Liu, and C. M. Hsu, *J. Comput. Phys.* **178**, 464 (2000).
- [17] R. J. Braun, B. T. Murray, *J. Cryst. Growth* **174**, 41 (1997).
- [18] R. Tonhardt, G. Amberg, *J. Cryst. Growth* **213**, 161 (2000).
- [19] J.-H. Jeong, N. Goldenfield, and J. A. Dantzig, *Phys. Rev. E* **64**, 041602 (2002).
- [20] M. J. Aziz and T. Kaplan, *Acta Metall.* **36**, 2335 (1988).
- [21] N. A. Ahmad, A. A. Wheeler, W. J. Boettinger, and G. B. McFadden, *Phys. Rev. E* **58**, 3436 (1998).
- [22] G. P. Ivantsov, *Dokl. Akad. Nauk SSSR* **558**, 576 (1947).
- [23] H. Fredriksson, N. El. Mahallawy, M. Taha, Lin Xiang, and G. Wang Low, *Scand. J. Metall.* **5**, 127 (1986).
- [24] Ph. Bouissou and P. Pelce, *Phys. Rev. A* **40**, 6673 (1989).
- [25] D. A. Kessler and H. Levine, *Phys. Rev. B* **33**, 7687 (1986).
- [26] J. Lipton, M. E. Glickson, and W. Kurz, *Metall. Trans. A* **18**, 341 (1987).